Self-powered retractable reel sensor for crack monitoring and warning in civil infrastructures

Xiaole Cao [a,b], Xuelian Wei [a,b], Xiaoqing Huo [a,b], Baocheng Wang [a,b], Yiran Hu [a,b], Zhong Lin Wang [a,c,d,*], Zhiyi Wu [a,b,*]

[a] *Beijing Institute of Nanoenergy and Nanosystems, Chinese Academy of Sciences, Beijing 101400, PR China*
[b] *School of Nanoscience and Technology, University of Chinese Academy of Sciences, Beijing 100049, PR China*
[c] *School of Materials Science and Engineering, Georgia Institute of Technology, Atlanta, GA 30332, USA*
[d] *Yonsei Frontier Lab, Yonsei University, Seoul 03722, Republic of Korea*

ARTICLE INFO

ABSTRACT

Crack occurrence and propagation are among the critical factors that affect the performance and lifespan of civil infrastructure such as bridges, buildings, etc. Therefore, numerous crack detection and characterization techniques have been developed over the past decades. In this study, we proposed the self-powered with the merits of cost-affordable, high resolution, and wide monitoring range to monitor small cracks in infrastructure. The self-powered retractable reel sensor includes two triboelectric nanogenerator (TENG) sensing units for low and high speed fracture monitoring, respectively. By using the principle of retractable reel structure, the linear motion of the crack is converted into the rotation of the TENG. Through peak extraction and pulse counting, the testing of crack velocity and displacement was realized simultaneously. A real resolution of 0.222 mm are achieved through the structural design and electrical performance characterization. With the help of the LabVIEW platform and multi-channel data acquisition program, its application in crack monitoring and early warning is successfully demonstrated. This work presents a novel self-powered sensor for crack monitoring and early warning, such a strategy is potentially available for distributed sensor construction towards structural health monitoring (SHM) of the infrastructure.

1. Introduction

Civil infrastructure (such as bridges, etc.) typically plays an important role in the prosperity of a society [1]. Tragic disasters that take an enormous toll on human life and property, such as bridge and building collapses, have frequently occurred due to small cracks in the infrastructure [2,3]. Typically, the crack formation process is relatively slow, but it can develop rapidly along the solid structure of the infrastructure once it is formed [4,5]. Therefore, timely detection of cracks after their initiation through dynamic crack monitoring is essential to mitigate or prevent catastrophes. Structural Health Monitoring (SHM) methods have been widely used to assess the performance of these structures and to detect damage at an early stage [6–8]. Intelligent sensor networks are the core of SHM systems, and sensing technologies such as resistance sensors, capacitive sensors, piezoelectric membranes, and fiber optics are typically used for crack monitoring [9–13]. However, these methods are limited by low resolution, complex installation, high maintenance

costs, or difficulty in using for continuous monitoring. Non-destructive testing techniques such as acoustic emission can also be used for the identification and location of structural damage [14,15]. Alternatively, the use of vision-based techniques such as photogrammetry, or laser scanning for a one-time inspection, and combined with analysis by technical means such as artificial intelligence image recognition, can yield quantifiable key information [16,17]. However, these technologies often require expensive equipment and skilled technicians to operate and cannot be implemented on a large scale.

Recently, there has been an increasing interest in developing self-powered sensing and monitoring methods for infrastructure systems [18,19]. A large number of studies are currently using piezoelectric materials as their sensing units [20–22]. However, their output voltage signals are relatively small so that are easily affected by environmental noise. Triboelectric nanogenerator (TENG) was first invented by Wang's group in 2012 and has proven to be a promising technology for mechanical energy harvesting and self-powered sensing [23–27]. TENG

generates electrical signals based on the triboelectric effect and electrostatic induction in response to external mechanical stimuli, which can also be used as an active sensor. On the other hand, the sensor based on TENG can also use the generated electric energy for a self-powering supply. Since their discovery, TENGs have attracted attention due to their low cost, diverse structures, and stable output performance [28–32]. Several attempts to develop self-powered crack monitoring have been reported as follows: Jung et al. developed a wire-based triboelectric resonator for crack detection by vibrating a metal wire on a dielectric film, to obtain the resonant frequency of the self-powered triboelectric outputs, so that to monitor the crack formation and spreading. However, it often needs to provide a vibration frequency that affects its autonomous and stable continuous monitoring [33]. Zhang et al. proposed multifunctional triboelectric nanogenerator-enabled structural elements for infrastructure monitoring systems [34], but they only proposed concepts for next-generation infrastructure monitoring that are not really applied in practice. Consequently, there is still a lack of self-powered fracture detection devices that are reliable, convenient, and have a high resolution.

Here, based on the newly developed TENG technology and the retractable reel structure, we report the self-powered retractable reel sensor with the merits of lightweight, cost-affordable, high resolution and wide monitoring range for monitoring the crack and early warning in infrastructure. The proposed retractable sensor contains two TENG sensing units (TENG-L, TENG-H), each of which in turn contains two TENGs (TENG-L_1, L_2, and TENG-H_1, H_2). The electrical signal generated by the TENG sensing unit is used for feedback information without other external power supplies. Through the structural design and electrical performance characterization, TENG-L, and TENG-H sensing units were determined for low and high-speed fracture respectively. And we introduce the TENG-L_2 and H_2 as the reference TENG respectively, so as to achieve the real resolution of 0.218 mm of the self-powered retractable reel sensor. Finally, its application in crack monitoring and early warning is successfully demonstrated using the LabVIEW platform and multi-channel data acquisition program. And the sensing signal has good adaptability in a wide range of temperatures and humidity. Our study establishes a new generation of self-powered crack monitoring sensors, which has wide applications in dynamic monitoring of bridges, houses, and other infrastructure.

2. Experimental Section

2.1. Fabrication of the retractable reel sensor

The fabrication of the sensor is mainly based on the mature technology of 3D printing and printed circuit board (PCB) technology. The retractable reel sensor has been made through 3D printing equipment to print out the shell. Draw processing drawings of the grating electrode and interdigital electrode (Cu, 50 μm thick) through Shapr 3D software, and commercially produce PCBs as stator and rotor of TENG, the exact dimensions of the PCBs are shown in Fig. S3 (Supporting information). The FEP film (20 μm thick) is applied to the interdigital electrode as a dielectric negative material and the grating electrode serves as a positive triboelectric layer dielectric material. The retractable reel structure is a commercially produced component. Finally, according to the order of shell, interdigital electrode PCB, grating electrode PCB, reel, grating electrode PCB, interdigital electrode PCB, shell, coaxial assembly add fixed with screws.

2.2. Electrical measurements

All measurements of the retractable reel sensor were performed using the programmable electrometers (Keithley Instruments model 6514). A stepper motor (86HSE8.5 N, China) is used to drive the TENG when testing the electrical performance. The temperature and humidity measurements with temperature and humidity test chamber. Linear

motor (LinMot, BF01-37) is used to simulate crack fracture. Developing self-powered crack monitoring and warning system on the NI LabVIEW platform with a multichannel data acquisition program.

3. Results and discussion

3.1. Working mechanism and structure

To reduce or prevent tragic disasters such as bridge and building collapses, we proposed a self-powered retractable reel sensor to monitor small cracks in infrastructure. Benefiting from its salient features of lightweight and low cost, it is capable of being incorporated with infrastructure on a large scale. Fig. 1a shows the working architecture of the self-powered crack monitoring and warning system, which consists of a retractable reel sensor unit, a signal processing unit, and an early warning feedback unit. Specifically, as shown in Fig. 1b, the retractable reel sensor senses the crack information, and the signal processing unit collects the sensor output signal, obtains the sensing information after waveform analysis and calculation, and determines whether there is a risk. If a risk is present, a warning signal is triggered by the warning unit. The construction of the self-powered retractable reel sensor is based on the triboelectric nanogenerator (TENG) technology. By combining a retractable badge reel and two freestanding layer mode TENGs (TENG-H and TENG-L) that are suitable for high-speed fracture and low-speed fracture respectively. The physical difference between the two sensing units TENG L and TENG H is the difference in the number of interdigital electrodes, which leads to different monitoring sensitivities, and a small-volume and high-precision stretch sensor has been developed for crack monitoring. Specifically, Fig. 1c shows the exploded view of the retractable reel sensor, which consists of a 3D printed shell, a rotor part, and two stator parts that are coaxially assembled. The rotor part is made up of a retractable reel and two commercial printed circuit boards (PCBs) with two groups of grating electrodes (Cu, 50 μm thick), the two PCBs are bonded coaxially to the reel. The real pictures of internal retractable reel structure of the sensor are shown in the Fig S1 (Supporting information). When in the initial state, the rope is wrapped around the outside of the reel and isn't stretching, the coil spring is bound in the reel, which passes through a fixed shaft in the center of the housing. When stretching the rope, the coil spring will start to compress around fixed shaft in the center under the pull of the rope until it is compressed to the final state, at which time the rope displacement reaches a maximum value of 45 cm (Fig. S2, Supporting information), indicating that it can monitor a crack width of up to 45 cm. when releasing the rope, the rope will be rewound on the reel under the action of the coil spring.

Take TENG-L as an example, the stator part of TENG-L was shown in Fig. 1d, consists of two different interdigital electrodes, called TENG-L_1 and TENG-L_2. The difference in the overlaps of electrodes between TENG-L_1 and L_2 is designed to generate a set of quadrature signals for sensing and further increase the sensing resolution. According to the TENG periodicity results and sensing requirements, the two groups of electrodes differ by 1/4 cycle from each other (TENG-H_1 and H_2 are also similar). And the stators are two commercial PCBs with two groups of interdigital electrode structure (Cu, 50 μm thick), covered by fluorinated ethylene propylene (FEP, 20 μm thick) as the triboelectric dielectric membrane. The specific processing dimensions of PCB are shown in Fig. S3 (Supporting information). The grating electrodes on the rotor, interdigital electrodes on the stator, and the FEP membrane form a freestanding TENG, a detailed description of the fabrication process is available in the Experimental Section. The difference between TENG-L and TENG-H is the center angle difference of the grating electrodes, which determines the sensitivity of the sensor. Here, the number of interdigital electrode pairs is 90 for TENG-L and 15 for TENG-H, the details are discussed below.
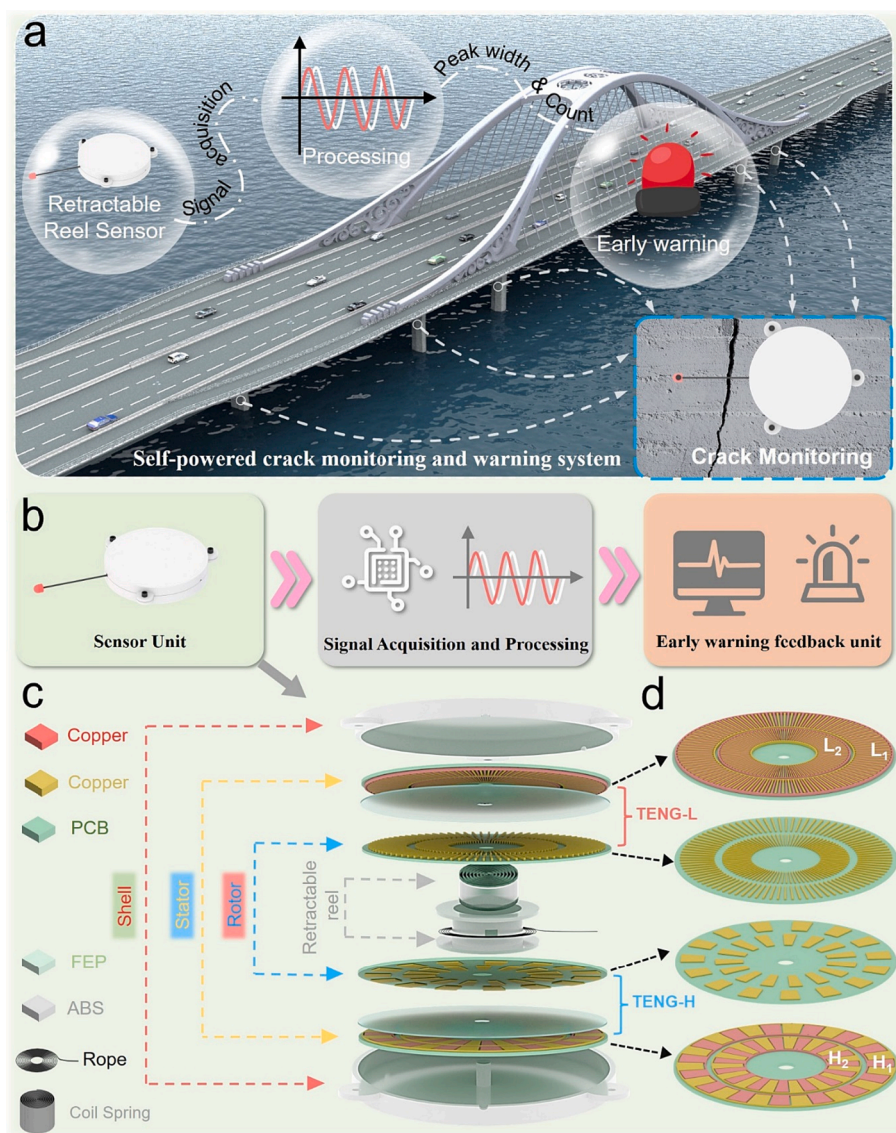
Fig. 1. Concept illustrations of the self-powered crack monitoring and warning system. (a) Schematic diagram of the self-powered crack monitoring and warning system, retractable reel sensor collects signals in real-time and process them for early warning, and insert is the schematic diagram of the retractable reel sensor installation position. (b) Workflow diagram of the self-powered crack monitoring and warning system. (c) Exploded view of the retractable reel sensor, consisting of a 3D printed shell, the stator, and the rotor (coil spring, TENGs, and rope). The whole retractable reel sensor includes two TENG sensing units (TENG-L and TENG-H). (d) Enlarged view of grating electrodes and interdigital electrodes of TENG-L and TENG-H.

3.2. Working principle and electrical characteristics of the TENG sensing units

The core sensing unit of the retractable reel sensor is the TENG, which couples the principles of triboelectricity and electrostatic induction. A part of TENG-L_1 and L_2 is selected to elucidate the working principle of the clockwise-rotated TENG-L sensing unit under short-circuit conditions. As shown in Fig. 2a and b, during the clockwise rotation triggered by the external, freestanding grating electrodes and FEP membrane are in good contact, and are positively charged by triboelectrification, with an equal number of negative charges generated on the FEP membrane. The negative charges on the FEP surface gradually accumulated and reached saturation after several cycles. Exemplified by TENG-L_1, Fig. 2a shows a typical working cycle of the freestanding TENG, only one basic unit of signal generation is introduced to clarify the working mechanism. The grating electrode is placed precisely above the left electrode of the interdigital electrodes, which is taken as the initial condition. The electrostatically induced negative

charges accumulate on the left electrode to balance the excessive positive polarization above it, while the right-hand electrode is positively charged by the same amount in the initial state. The clockwise rotation of the rotor and stator is caused by the stretching process redistributing the free electrons by flowing from the left electrode to the right electrode through the external circuit. As the grating electrode further and completely passes through the right electrode, the electrons flow back to the left electrode, generating a reverse current pulse through the external resistor. Owing to the difference in overlap, the freestanding grating electrode in TENG-L_2 is ahead of that in TENG-L_1, forming a detectable phase difference (φ) between the two signals. By controlling the size of the phase difference, a more sensitive sensing signal can be obtained. As shown in Fig. 2b, the finite element method (COMSOL Multiphysics) performs corresponding simulations of the open-circuit potential distribution under the entire rotation process, to observe the power generation process. We can clearly see that the potential of one electrode reaches its maximum when the freestanding grating electrode is precisely above it [35,36]. The overall working principle of TENG-H is
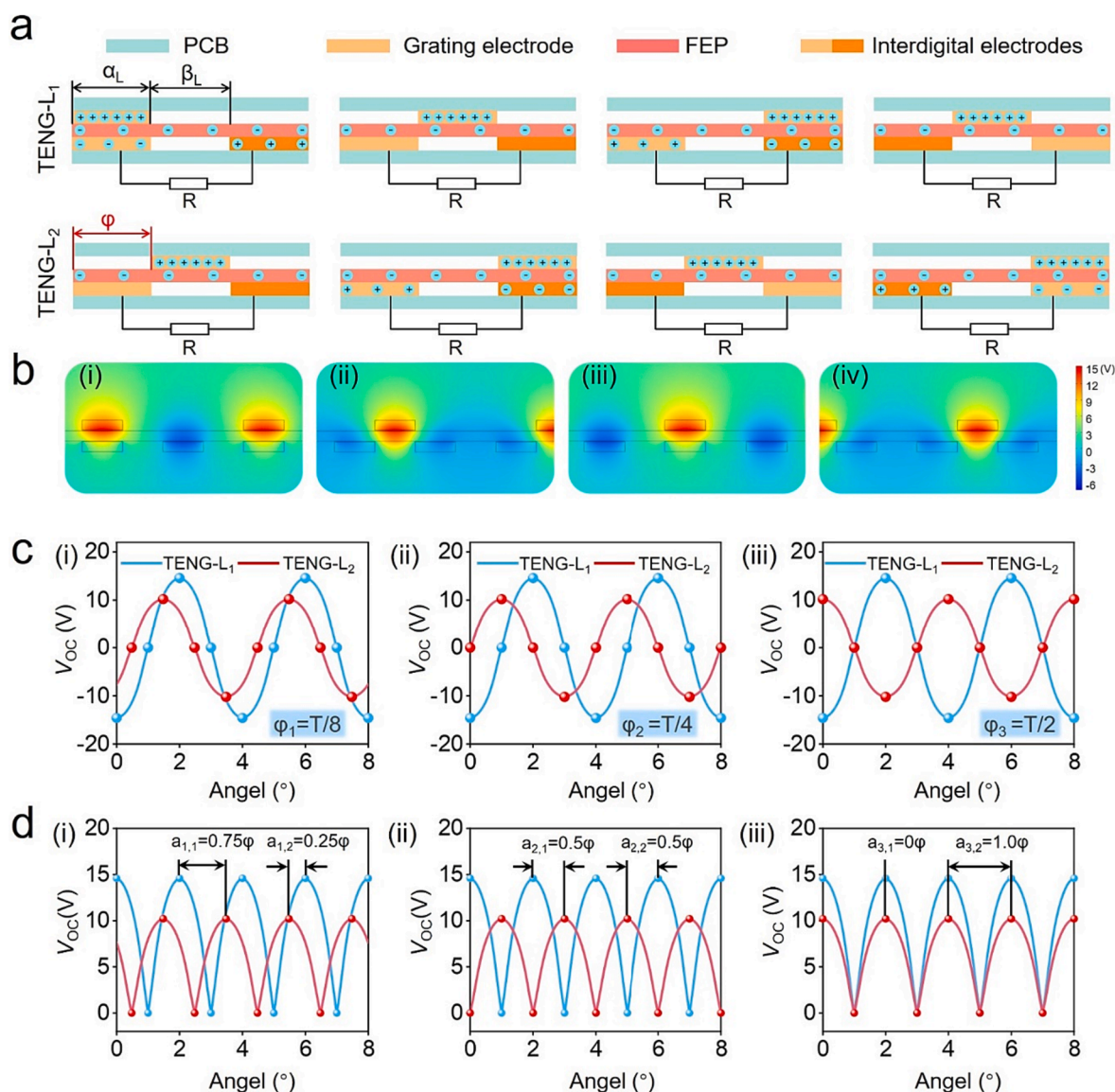
Fig. 2. The working principle of the retractable reel sensor. (a) Schematics of the operating principle of TENG-L (including L_1 and L_2) under short circuit condition, 1/4 cycle interval between L_1 and L_2. (b) COMSOL simulation results of TENG-L_1 corresponding to the rotating state. (c) Simulated variances of open circuit voltages of clockwise rotated TENG-L_1 and L_2 when the interval periods of L_1 and L_2 are T/8 (i), T/4 (ii), and T/2 (iii) respectively. (d) Simulated open-circuit voltage of TENG-L_1 and L_2 after rectification with clockwise rotation.

similar (Fig. S4, Supporting information), but the difference lies in the different center angles of the grating electrode (α) and that between the grating electrodes (β). As the center angle of the grating electrode increases (it is actually the increase of contact area), the peak-to-peak value of the sensing signal of TENG gradually increases [37].

Fig. S5 (Supporting information) plots out the simulated open circuit voltage (V_{OC}) between the interdigital electrodes as the grating electrode slides, showing a periodic voltage waveform. It is also worth noting that, when the grating electrode rotates through an angle of $\alpha + \beta$, the V_{OC} reverses, shifting from the peak to the valley, or the valley to the peak, meaning a half-period. Therefore, when the number of wave peaks or valleys is used as sensing information, the overall rotation angle can be calculated by counting the number of half periods T, and $\alpha + \beta$ stands for the minimum resolution. Subsequently, the resolution can be further improved by the phase difference of the two sensing signals of TENG-L_1 and TENG-L_2. Fig. 2c shows the simulated variances of V_{OC} of clockwise rotated TENG-L_1 and L_2 when the phase difference is T/8 (i), T/4 (ii) and T/2 (iii) respectively. During sensing signal processing, the signal is often rectified, where the valley is converted to a peak. The

corresponding voltage signal is shown in Fig. 2d. At this time, the peak phase difference of TENG-L_1 and L_2 is selected to be T/4 through comparison, and the minimum resolution is $(\alpha + \beta)/2$. Considering the size and processing of the TENG sensing unit, the final electrode center angle of TENG-L is $1°$, while that of TENG-H is $11°$, and that between the grating electrodes is both $1°$. In addition, the introduction of the phase difference not only improves the resolution, but can also be used to determine the direction of rotation. At this point, TENG-L_2 is used as the reference TENG for improving the resolution (similar to the TENG-H_2).

Fig. 3a shows the waveforms of TENG-L_1 and TENG-L_2 with resistance connected in series measured simultaneously, with anti-clockwise and clockwise rotation indicated on the left and right of the enlarged image, respectively. The signals belonging to TENG-L_1 and TENG-L_2 are regarded as sensing signals, and are plotted in blue and red, respectively. Similarly, using the peak of the waveform as a reference point, it can be seen that the phase difference between clockwise and anti-clockwise is T/4 and 3 T/4 respectively, which can be used as a criterion to judge the direction of rotation. For example, when the phase difference of T/4 is defined as a forward movement, then T3/4 is a reverse movement. And
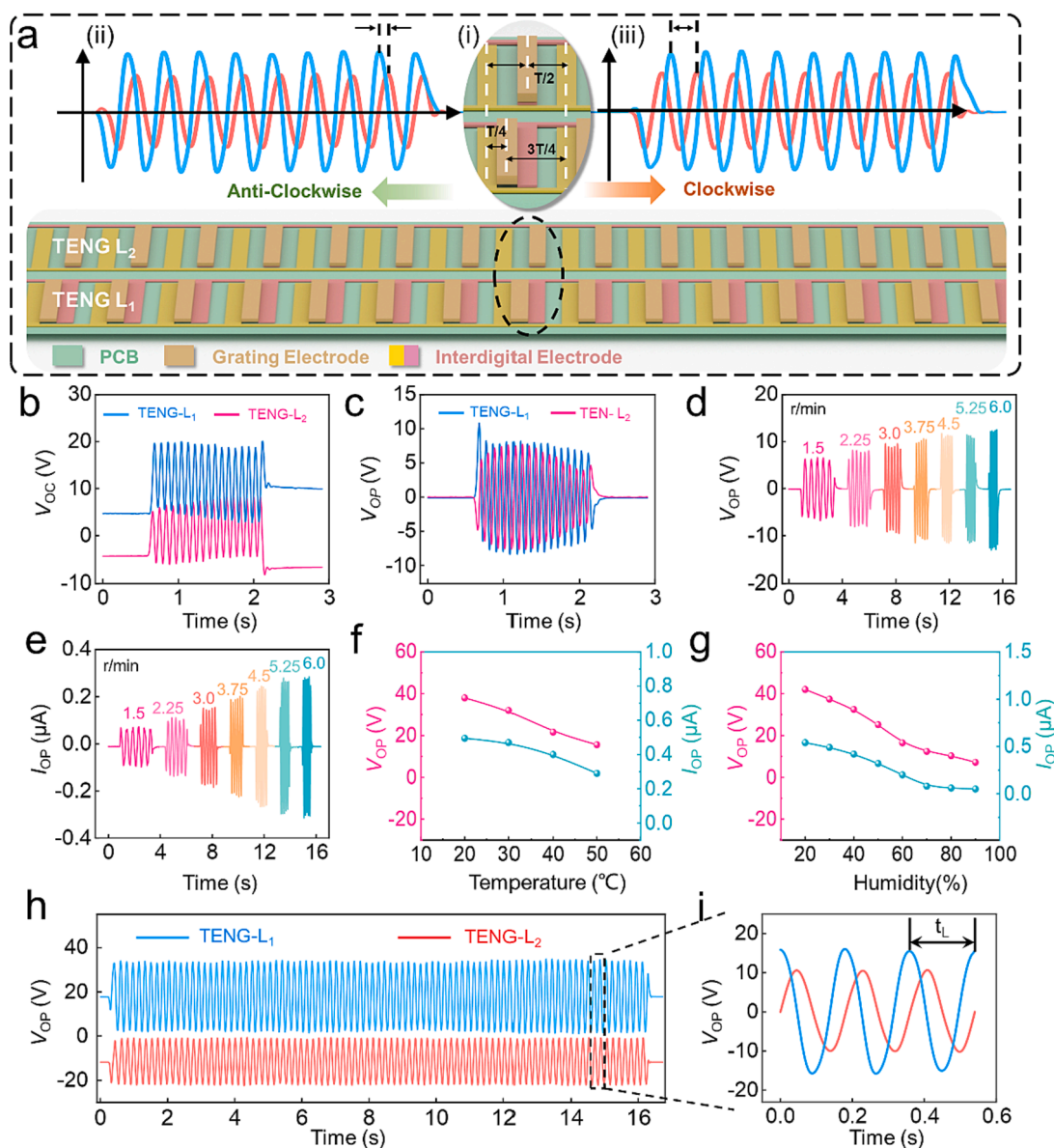
Fig. 3. Characterization of rotary TENG-L. (a) The structure and working mechanism of TENG-L sensor. inserted image (i) is an enlarged view of the interdigital electrode pair and a schematic of the period difference between TENG-L_1 and TENG-L_2, inserted images (ii) and (iii) show the open circuit voltage signals when TENG-L_1 and TENG-L_2 are rotated anti-clockwise and clockwise, respectively (b) The open circuit voltage waveforms generated by TENG-L_1 and L_2 when TENG-L is rotated anti-clockwise. (c) The voltage signals generated by TENG-L_1 and L_2 after connected a resistor in series when TENG-L is rotated clockwise. Variation of voltage (d) and current (e) of TENG-L_1 sensor with different rotational speeds. Variation of output voltage and current of TENG-L1 sensor with temperature (f) and humidity (g). (h) Voltage signal of the TENG-L_1 and TENG-L_2 sensors during a complete rotation cycle. (i) Enlarged views of distinct phase differences between TENG-L_1 and L_2.

the enlarged image shows the relative positions of the freestanding grating electrodes of the two TENGs, it should be noted that the main purpose here is to show the relative position of the grating electrodes, so the FEP film is not shown.

Afterward, the electrical performance of the TENG-L sensing unit was tested with the electrostatic meter. Initially, as shown in Fig. 3b, the V_{OC} signal is a standard square wave signal when the TENG has no series resistor. As shown in Fig. 3c, by connecting a resistor in series, the sensing signal (Voltage output, V_{OP}) is transformed into an AC signal similar to the short-circuit current (I_{SC}, Fig S6, Supporting information), which enables the subsequent processing of the sensing information. Due to the high internal resistance of TENG, which leads to the electrical characteristics of low current. Therefore, the voltage signal has a higher signal-to-noise ratio when used as a sensing signal. Fig. 3d,e, and S7 (Supporting information) show the variation of V_{OP} and I_{OP} (Current

output) of the TENG-L_1 sensor with different rotational speeds. As the rotational speed increases, the V_{OP} and I_{OP} of the TENG-L_1 sensor both increase gradually. The main reason is that for the same amount of transferred charge, the speed increases, the practice of electron transfer between external loads is shortened, and the current subsequently increases. It is worth noting that according to the theoretical model of the independent layer TENG, the V_{OP} is independent of frequency and speed, but we have connected an external resistor of 100 MΩ in series during the voltage measurement, so the V_{OP} increases as the I_{OP} increases. In addition, as a crack monitoring sensor, the electrical output of the device is inevitably affected by the ambient temperature and humidity during long-term operation. In this regard, taking TENG-L_1 as an example, the effect of temperature and humidity on the TENG sensing unit was investigated. As shown in Fig. 3f and g, both V_{OP} and I_{OP} decrease slightly with the increase of temperature and humidity. Considering the

normal ambient temperature as well as the humidity range, the output performance is degraded, but the voltage signal sensing information depends mainly on the peak spacing and period and is independent of the peak-to-peak value. The sensing signal at high temperature and high humidity can still be detected. On the other hand, the data presented here is primarily test data from a single TENG. In actual applications, the environmental impact on the device performance can be further reduced by packaging the device, so that the sensor can still provide accurate sensing information under different temperatures and humidity. Fig. 3h shows the generated V_{OP} signal of the TENG-L_1 and TENG-L_2 sensors during the whole cycle (360°) of anti-clockwise rotation. Obviously, when the TENG-L sensor unit rotates for one revolution, 180 periodic pulses are collected (and the pulses of the TENG-H sensor unit are 30). And Fig. 3i shows the view of distinct phase differences between TENG-L_1 and L_2. The electrical performance of the TENG-H sensing unit is shown in Fig. S8 and S9 (Supporting information).

3.3. Electrical characteristics of the self-powered retractable reel sensor

In the previous part, the electrical performance of TENG-L and H sensing units was explored. Subsequently, the TENG-L, H sensing units, retractable reel, and shell were coaxially assembled and fixed with screws to form the entire retractable reel sensor. The photograph and size of the retractable reel structure are shown in Fig. S10 (Supporting information), which consists of a rope, coil spring, and a reel. The rotation of the TENG is successfully transformed into a reciprocal translation motion through the retractable reel structure, thus a speed and displacement sensor are formed. The inner diameter of the reel is 25.0 mm. At this time, the calculation formula of velocity v and displacement L is rough as follows:
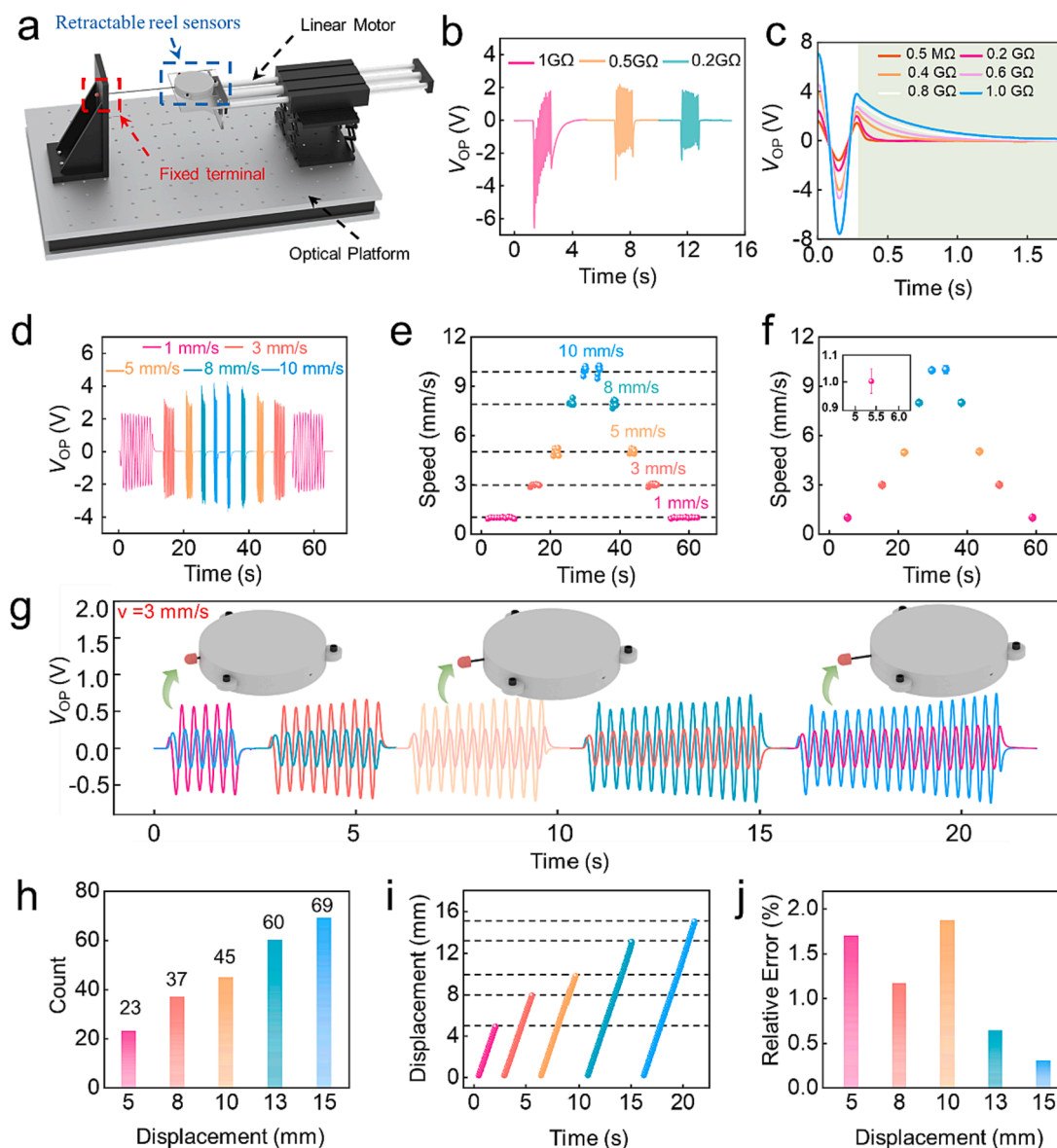

Fig. 4. Details analysis of sensing signals of the retractable reel sensor. (a) Schematic diagram of the retractable reel sensor test platform. (b) Dragging phenomenon of output voltage with different resistors connected in series. (c) Output voltage curve of TENG-L_1 in series with different resistors. (d) Output voltage signal of TENG-L_1 unit of the retractable reel sensor at different stretching speeds with the same displacement (10 mm). (e) Calculated stretching speeds from the experiment data in the diagram (d). (f) The average speed and the standard deviation are calculated from the experimental data in the diagram (d). (g) Output voltage signal of TENG-L unit of the retractable reel sensor at a speed of 3 mm·s^{-1} with different displacement, insert images are corresponding stretch states of the retractable reel sensor. (h) Calculated number of peaks and valleys from the experiment data in the diagram (g). (i) Calculated displacement from the experiment data in the diagram (g). (j) Absolute error of the calculated displacement.

$$v = \frac{\pi D}{n\, t_{avg}} \tag{1}$$

$$L = \frac{\pi D}{n} n_{count} \tag{2}$$

where D represents the diameter of the reel, and the number of waves generated by one rotation of the grating electrode is defined as n, t_{avg} is the average value of wave peak width, and n_{count} is the number of wave peaks generated by one TENG when moving a displacement. At this point for the TENG-L$_1$, no matter where the initial position starts, as long as the displacement increases by 0.872 mm, the curve of the measured voltage signal will span a complete cycle, therefore, the total displacement can be obtained by counting the number of pulses. Since the introduction of the reference signal of TENG-L$_2$ and the half-wave rectification unit, the number of wave crests will be increased from one to four, thus increasing the displacement resolution to 0.218 mm.

As shown in Fig. 4a, a simulated displacement test platform on the optical platform was established to systematically characterize the retractable reel sensor under various motion conditions. A multichannel synchronous data acquisition system was employed to acquire signals produced by two or more TENGs simultaneously. The multichannel synchronous acquisition system can only collect sensing signals within 10 V, different resistors are connecting in series to divide the voltage and thus narrow the sensing signals. As illustrated in Fig. 4b, in the process of achieving voltage division, the sensing signal produces a tailing effect because of the excessive resistance, which can be considered as excessive resistance impeding the flow of electrons, and the sensing signal is distorted when the speed is too fast. Fig. 4c compares the trailing effect of different resistances on the sensing signal. As the resistance is reduced from 1 GΩ to 0.5 MΩ, the time taken for the voltage signal to recover to the baseline decreases from 1.45 s to 0.11 s. Taking into account the peak voltage value of the sensing signal as well as the stability of the signal, a resistance of 0.2 GΩ was finally chosen for the subsequent measurement.

Fig. 4d shows the output voltage signals of the TENG-L$_1$ of the retractable reel sensor for the same displacement of reciprocating motion at different stretching speeds (the corresponding signal of TENG-L$_2$ is shown in Fig. S11, Supporting information). As shown in Fig. 4d, an identical number of voltage pulses of 12 was obtained under all velocities with an overall displacement of 10 mm, which suggests an irrelevance between the number of signal pulses and the angular velocity. Afterward, as shown in Fig. 4e, stretching speeds are calculated with data plotted in Fig. 4d via the above-mentioned strategies, inserted dashed lines denote pre-set stretching speeds. Take the 1 mm·s^{-1} speed data as an example, calculated stretching speeds fluctuate around the pre-set one with an averaged velocity of 0.992 mm·s^{-1} and a standard error of 0.033 mm·s^{-1}. Fig. 4f shows the calculated average and standard deviation of different speeds, and the specific data are shown in Table S1 (Supporting information). It is found that the corresponding standard deviation is relatively large at high velocity, and this is still mainly due to the trailing effect caused by the hindering effect of the resistance on the electrons. Subsequently, the performance of the retractable reel sensor used as the displacement sensor is characterized. As illustrated in Fig. 4g, the output voltage signals of the TENG-L unit of the retractable reel sensor at a speed of 3 mm·s^{-1} with different displacements were measured, and insert images are corresponding stretch states of the retractable reel sensor. Unlike the speed sensor, the displacement calculation requires the waveform signals of the entire unit of TENG-L. The number of wave peaks of the rectified signal is shown in Fig. 4h. Based on this, as shown in Fig. 4i, displacements are calculated with data plotted in Fig. 4g and h via the above-mentioned strategies, inserted dashed lines denote pre-set stretching displacements. Similarly, the corresponding absolute error is shown in Fig. 4j and Table S2. As mentioned above, the TENG-L sensing unit is used to detect cracks in low-speed motion (v < 10 mm·s^{-1}, that could obtain a

high degree of accuracy), while TENG-H can be used to detect high-speed motion. Together, the two sensing units form a retractable reel that cooperates with each other to achieve a higher detection range. The characterization of the TENG-H sensing unit is shown in Fig. S12, and Table S3, 4 (Supporting information).

3.4. Demonstration of the crack monitoring and early warning

Presented in Fig. 5 is the self-powered crack monitoring and warning system developed on the LabVIEW platform with the multichannel data acquisition program. Fig. 5a shows the sensor signal processing logic and workflow diagram of the self-powered system based on LabVIEW platform. Specifically, the analog signal generated by the sensor was converted into a digital signal by the multi-channel acquisition program, and then low-pass filtering is performed. After peak extraction of the sensed signal, the wave width is obtained and the stretching velocity is calculated. The results of the corresponding sensing unit, including velocity and displacement, are output after comparison with the set threshold. On the other hand, the sensing signal is rectified and the peak value is extracted to obtain the number of peaks and then stretching displacement was calculated. By comparing with the set crack width threshold, once the set value is exceeded, the alarm system will be activated. It should be noted that the TENG-L sensing unit is often used for routine detection and early warning to guide the repair work, while TENG-H is used for sudden fracture and timely alarm, so as to provide rapid rescue for the rescue team and carry out rescue work. Here, we set a speed threshold of 10 mm·s^{-1}. Fig. 5b illustrates the data processing process of corresponding sensing signals.

As shown in Fig. 5c, the crack fracture process was simulated on the optical platform, and the application of self-powered crack monitoring and early warning was demonstrated. When the crack speed is 3 mm·s^{-1}, the TENG-L sensing unit outputs the corresponding speed and fracture displacement, and the alarm signal is issued when the set width of 20 mm is exceeded (Movie S1, Supporting information). The sensor measured 90 peaks and the minimum resolution calculated at this point is 0.222 mm. Fig. 5c iii and iv show the processing of the output signal of the TENG-L sensing unit. When the crack fracture speed is greater than 10 mm·s^{-1} (Fig. S13 and Movie S2 Supporting information), the TENG-H sensing unit outputs the signal and the alarm is sounded to notify emergency rescue. The way to carry out crack monitoring in practical applications consists of spot monitoring of cracks that have already been created. According to the occurrence of small cracks in the area, the direction of cracks placed sensors to prevent further harm. The second is the point monitoring method, for the structure by analyzing the stress distribution, theoretical prediction of the key point location to place sensors to monitor, this situation through the location of the fracture prone to stress analysis, scientific placement of crack detection sensors.

4. Conclusion

In summary, the self-powered retractable reel sensor based on the TENG technology was proposed to monitor small cracks in infrastructure, so as to reduce or prevent tragic disasters such as bridge and building collapses. The proposed retractable sensor contains two TENG sensing units (TENG-L, TENG-H), each of which in turn contains two TENGs (TENG-L$_1$, L$_2$, and TENG-H$_1$, H$_2$). Through the structural design and electrical performance characterization, TENG-L, and TENG-H were determined for low and high-speed fracture respectively. By using the reel structure, the linear motion of the crack is converted into the rotation of the TENG, and the monitoring of crack velocity and displacement was realized simultaneously by peak extraction, and pulse counting of the sensing signals. On this basis, the sensing signal has good adaptability in a wide range of temperatures and humidity. By introducing the TENG-L$_2$ and H$_2$ as the reference TENG respectively, the real resolution of 0.222 mm of the self-powered retractable reel sensor are achieved. Finally, with the help of the LabVIEW platform and
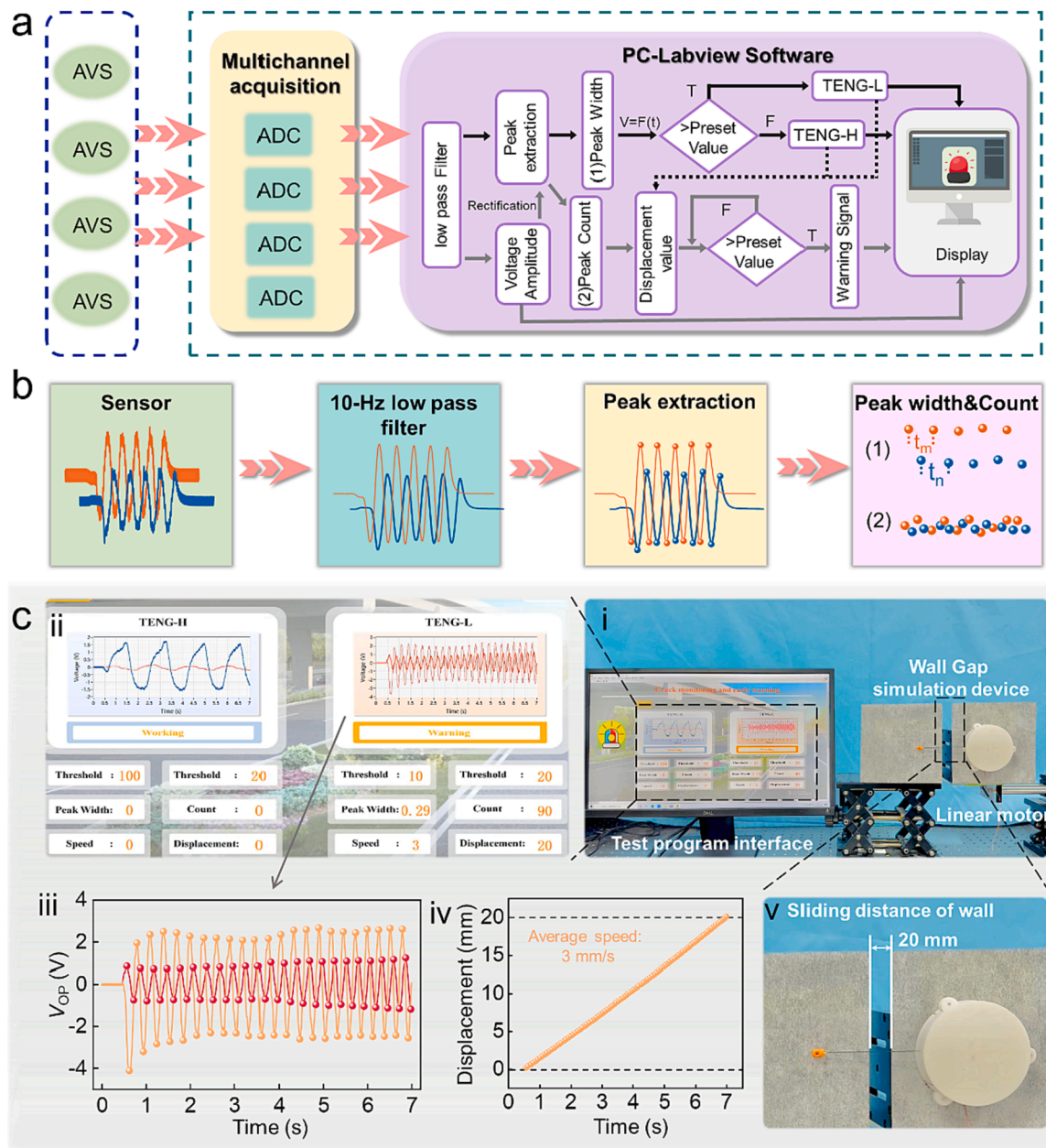
Fig. 5. Demonstration of the self-powered retractable reel sensor for crack monitoring and early warning. (a) Detail logic and workflow diagram of the self-powered crack monitoring and warning system based on the LabVIEW platform. (b) Schematic diagram of the signals processing process of the retractable reel sensor. (c) Application demonstration of the self-powered crack monitoring and warning system during low-speed fracture. (i) Photograph of the simulated crack monitoring platform. (ii) Monitoring signals of the retractable reel sensor during high-speed fracture in the crack simulation test. (iii) Signal amplification diagram of TENG-L sensor unit. (iv) Calculated displacement from the experiment data in the diagram (iii). (v) Optical photograph of simulated crack fracture.

multichannel data acquisition program, its application in crack monitoring and early warning is successfully demonstrated. The proposed retractable reel sensor exhibits merits of both cost-affordable, and wide monitoring range. In the long run, it shows the application prospect of being the next generation of self-powered sensors for monitoring cracks or small deformations in civil infrastructures.

Declaration of Competing Interest

The authors declare that they have no known competing financial interests or personal relationships that could have appeared to influence the work reported in this paper.

Data availability

Data will be made available on request.

Appendix A. Supplementary data

Supplementary data to this article can be found online at https://doi.org/10.1016/j.cej.2023.147238.

References

[1] J.M. Brownjohn, Structural health monitoring of civil infrastructure, Philos. Trans. A Math. Phys. Eng. Sci. 365 (2007) 589–622, https://doi.org/10.1098/rsta.2006.1925.

[2] A. Farhidzadeh, E. Dehghan-Niri, A. Moustafa, S. Salamone, A. Whittaker, Damage assessment of reinforced concrete structures using fractal analysis of residual crack patterns, Exp. Mech. 53 (2013) 1607–1619, https://doi.org/10.1007/s11340-013-9769-7.

[3] K.J. Miller, The short crack problem, Fatigue Fract. Eng. Mater. Struct. 5 (1982) 223–232, https://doi.org/10.1111/j.1460-2695.1982.tb01250.x.

[4] R.O. Ritchie, Mechanisms of fatigue crack propagation in metals, ceramics and composites: Role of crack tip shielding, Mater. Sci. Eng., A, **103,**15-28 (1988). http://doi.org/10.1016/0025-5416(88)90547-2.

[5] D. Taylor, J.F. Knott, Fatigue crack propagation behaviour of short cracks; the effect of microstructure, Fatigue Fract. Eng. Mater. Struct. 4 (1981) 147–155, https://doi.org/10.1111/j.1460-2695.1981.tb01116.x.

[6] A. Kita, N. Cavalagli, M.G. Masciotta, P.B. Lourenço, F. Ubertini, Rapid post-earthquake damage localization and quantification in masonry structures through multidimensional non-linear seismic IDA, Eng. Struct. 219 (2020), https://doi.org/10.1016/j.engstruct.2020.110841.

[7] L.F. Ramos, L. Marques, P.B. Lourenço, G. De Roeck, A. Campos-Costa, J. Roque, Monitoring historical masonry structures with operational modal analysis: two case studies, Mech. Syst. Signal. Pr. 24 (2010) 1291–1305, https://doi.org/10.1016/j.ymssp.2010.01.011.

[8] Q. Zhang, K. Barri, S.K. Babanajad, A.H. Alavi, Real-time detection of cracks on concrete bridge decks using deep learning in the frequency domain, Engineering 7 (2021) 1786–1796, https://doi.org/10.1016/j.eng.2020.07.026.

[9] P. Ahuja, S. Akiyama, S.K. Ujjain, R. Kukobat, F. Vallejos-Burgos, R. Futamura, T. Hayashi, M. Kimura, D. Tomanek, K. Kaneko, A water-resilient carbon nanotube based strain sensor for monitoring structural integrity, J. Mater. Chem. A 7 (2019) 19996–20005, https://doi.org/10.1039/c9ta06810d.

[10] T. Lee, Y.W. Choi, G. Lee, P.V. Pikhitsa, D. Kang, S.M. Kim, M. Choi, Transparent ITO mechanical crack-based pressure and strain sensor, J. Mater. Chem. C 4 (2016) 9947–9953, https://doi.org/10.1039/c6tc03329f.

[11] Y. Song, X. Liu, D. Zhang, X. Fan, R. Cui, Y. Zheng, Y. Wang, A grating coating sensor for quantitative monitoring of metal structure cracks under varying ambient temperature, Measurement 192 (2022), https://doi.org/10.1016/j.measurement.2022.110919.

[12] Y. Tang, Z. Wu, Distributed long-gauge optical fiber sensors based self-sensing FRP bar for concrete structure, Sensors (basel) 16 (286) (2016), https://doi.org/10.3390/s16030286.

[13] W.H. Duan, Q. Wang, S.T. Quek, Applications of piezoelectric materials in structural health monitoring and repair: selected research examples, Materials (basel) 3 (2010) 5169–5194, https://doi.org/10.3390/ma3125169.

[14] A. Carpinteri, G. Lacidogna, Damage Monitoring of an Historical Masonry Building by the Acoustic Emission Technique, Mater. Struct. 39 (2006) 161–167, https://doi.org/10.1617/s11527-005-9043-2.

[15] E. Verstrynge, K. De Wilder, A. Drougkas, E. Voet, K. Van Balen, M. Wevers, Crack monitoring in historical masonry with distributed strain and acoustic emission sensing techniques, Constr. Build. Mater. 162 (2018) 898–907, https://doi.org/10.1016/j.conbuildmat.2018.01.103.

[16] B. Riveiro, M.J. DeJong, B. Conde, Automated processing of large point clouds for structural health monitoring of masonry arch bridges, Autom. Constr. 72 (2016) 258–268, https://doi.org/10.1016/j.autcon.2016.02.009.

[17] R. Napolitano, B. Glisic, Methodology for diagnosing crack patterns in masonry structures using photogrammetry and distinct element modeling, Eng. Struct. 181 (2019) 519–528, https://doi.org/10.1016/j.engstruct.2018.12.036.

[18] H. Salehi, R. Burgueño, S. Chakrabartty, N. Lajnef, A.H. Alavi, A comprehensive review of self-powered sensors in civil infrastructure: State-of-the-art and future research trends, Eng. Struct. 234 (2021), https://doi.org/10.1016/j.engstruct.2021.111963.

[19] K.M. Farinholt, N. Miller, W. Sifuentes, J. MacDonald, G. Park, C.R. Farrar, Energy Harvesting and wireless energy transmission for embedded SHM sensor nodes, Struct. Health Monit. 9 (2010) 269–280, https://doi.org/10.1177/1475921710366647.

[20] C.E. Chalioris, C.G. Karayannis, G.M. Angeli, N.A. Papadopoulos, M.J. Favvata, C.P. Providakis, Applications of smart piezoelectric materials in a wireless admittance monitoring system (WiAMS) to Structures—Tests in RC elements, Case. Stud. Constr. Mat. 5 (2016) 1–18, https://doi.org/10.1016/j.cscm.2016.03.003.

[21] H.P. Konka, M.A. Wahab, K. Lian, Piezoelectric fiber composite transducers for health monitoring in composite structures, Sensor Actuators a: Phys. 194 (2013) 84–94, https://doi.org/10.1016/j.sna.2012.12.039.

[22] X. Cao, Y. Xiong, J. Sun, X. Zhu, Q. Sun, Z.L. Wang, Piezoelectric nanogenerators derived self-powered sensors for multifunctional applications and artificial intelligence, Adv. Funct. Mater. 31 (2021), https://doi.org/10.1002/adfm.202102983.

[23] F.-R. Fan, Z.-Q. Tian, Z. Lin Wang, Flexible triboelectric generator, Nano Energy 1 (328–334) (2012), https://doi.org/10.1016/j.nanoen.2012.01.004.

[24] X. Cao, Y. Xiong, J. Sun, X. Xie, Q. Sun, Z.L. Wang, Multidiscipline applications of triboelectric nanogenerators for the intelligent era of internet of things, Mechanical Systems and Signal ProcessingNanomicro Lett 15 (2022) 14, https://doi.org/10.1007/s40820-022-00981-8.

[25] X. Cao, X. Wei, R. Li, Z. Wang, Z. Wu, Thermal-mechanical-electrical energy conversion system based on Curie effect and soft-contact rotary triboelectric nanogenerator, Nano Res. 16 (2022) 2502–2510, https://doi.org/10.1007/s12274-022-5056-1.

[26] Z. Zhu, H. Xiang, Y. Zeng, J. Zhu, X. Cao, N. Wang, Z.L. Wang, Continuously harvesting energy from water and wind by pulsed triboelectric nanogenerator for self-powered seawater electrolysis, Nano Energy 93 (2022), 106776, https://doi.org/10.1016/j.nanoen.2021.106776.

[27] L. Xie, N. Zhai, Y. Liu, Z. Wen, X. Sun, Hybrid triboelectric nanogenerators: from energy complementation to integration, Research 2021 (2021), https://doi.org/10.34133/2021/9143762.

[28] Y. Chen, Z. Gao, F. Zhang, Z. Wen, X. Sun, Recent progress in self-powered multifunctional e-skin for advanced applications, Exploration 2 (2022), https://doi.org/10.1002/exp.20210112.

[29] A. Leber, B. Cholst, J. Sandt, N. Vogel, M. Kolle, Stretchable thermoplastic elastomer optical fibers for sensing of extreme deformations, Adv. Funct. Mater. 29 (2018), 1802629, https://doi.org/10.1002/adfm.201802629.

[30] L. Ma, R. Wu, A. Patil, J. Yi, D. Liu, X. Fan, F. Sheng, Y. Zhang, S. Liu, S. Shen, J. Wang, Z.L. Wang, Acid and alkali-resistant textile triboelectric nanogenerator as a smart protective suit for liquid energy harvesting and self-powered monitoring in high-risk environments, Adv. Funct. Mater. 31 (2021), 2102963, https://doi.org/10.1002/adfm.202102963.

[31] Y. Pang, S. Chen, J. An, K. Wang, Y. Deng, A. Benard, N. Lajnef, C. Cao, Multilayered cylindrical triboelectric nanogenerator to harvest kinetic energy of tree branches for monitoring environment condition and forest fire, Adv. Funct. Mater. 30 (2020), 2003598, https://doi.org/10.1002/adfm.202003598.

[32] T. Zhang, Z. Wen, Y. Liu, Z. Zhang, Y. Xie, X. Sun, Hybridized Nanogenerators for Multifunctional Self-Powered Sensing: Principles, Prototypes, and Perspectives, iScience, 23, (2020). http://doi.org/10.1016/j.isci.2020.101813.

[33] Y. Jung, J. Yu, H.J. Hwang, D. Bhatia, K.-B. Chung, D. Choi, Wire-based triboelectric resonator for a self-powered crack monitoring system, Nano Energy 71 (2020), https://doi.org/10.1016/j.nanoen.2020.104615.

[34] Q. Zhang, K. Barri, S.R. Kari, Z.L. Wang, A.H. Alavi, Multifunctional triboelectric nanogenerator-enabled structural elements for next generation civil infrastructure monitoring systems, Adv. Funct. Mater. 31 (2021), https://doi.org/10.1002/adfm.202105825.

[35] N. Cui, J. Liu, L. Gu, S. Bai, X. Chen, Y. Qin, Wearable triboelectric generator for powering the portable electronic devices, ACS Appl. Mater. Interfaces 7 (2015) 18225–18230, https://doi.org/10.1021/am5071688.

[36] Z. Wang, J. An, J. Nie, J. Luo, J. Shao, T. Jiang, B. Chen, W. Tang, Z.L. Wang, A self-powered angle sensor at nanoradian-resolution for robotic arms and personalized medicare, Adv. Mater. 32 (2020), e2001466, https://doi.org/10.1002/adma.202001466.

[37] C. Li, D. Liu, C. Xu, Z. Wang, S. Shu, Z. Sun, W. Tang, Z.L. Wang, Sensing of joint and spinal bending or stretching via a retractable and wearable badge reel, Nat. Commun. 12 (2021) 2950, https://doi.org/10.1038/s41467-021-23207-8.